Palaeogeography, Palaeoclimatology, Palaeoecology 636 (2024) 111969

Contents lists available at ScienceDirect

Palaeogeography, Palaeoclimatology, Palaeoecology

journal homepage: www.elsevier.com/locate/palaeo

Biogeochemical responses to global warming during the Paleocene–Eocene Thermal Maximum in the eastern Tethys

Qingting Wu [a,*], Ying Cui [a,*], Yasu Wang [b], Shijun Jiang [b], Yixin Dong [c], Jun Shen [d]

[a] Department of Earth and Environmental Studies, Montclair State University, Montclair, NJ 07043, USA
[b] College of Oceanography, Hohai University, Nanjing 245700, China
[c] State Key Laboratory of Oil and Gas Reservoir Geology and Exploitation, Chengdu University of Technology, Chengdu 610059, China
[d] State Key Laboratory of Geological Processes and Mineral Resources, China University of Geosciences, Wuhan 430074, China

ARTICLE INFO

Editor: Dr. Howard Falcon-Lang

Keywords:
Paleocene–Eocene Thermal Maximum
Eastern Tethys
Marine productivity
Paleoclimate
Deoxygenation

ABSTRACT

The Paleocene–Eocene Thermal Maximum (PETM; ~56 Ma) represents a rapid and sustained climatic perturbation that lasted for ~170 kyr and coincided with the emplacement of the North Atlantic Igneous Province (NAIP). Global average temperature increased by 5 to 9 °C, which was likely triggered by a rapid emission of ^{13}C-depleted CO_2. Numerous sites from the deep oceans have been studied for the PETM, but subtropical shallow-water eastern Tethys remains poorly understood despite its importance in regulating heat and moisture transport. Prior studies on calcareous nannofossil biostratigraphy and stable isotopes of marine carbonates confirmed the occurrence of the PETM in the Tarim Basin of the eastern Tethys in northwestern China. Here we present new, high–resolution major, trace and rare earth element geochemical data, and clay mineral records at the Kuzigongsu section in the Tarim Basin to assess the biogeochemical responses of the eastern Tethys to climatic forcings across the PETM. Chemical weathering proxies (chemical index of alteration [CIA], chemical index of weathering [CIW], plagioclase index of alteration [PIA], and Rb/Sr) support an enhanced terrestrial input shortly after the PETM onset, possibly due to intensified chemical weathering. Furthermore, clay mineral assemblage is dominated by illite and illite/smectite during the PETM, implying increased physical weathering. The PETM is also characterized by an increase in nutrient-sensitive elements such as P, Ni, and Cu and higher abundance of nutrient–sensitive calcareous nannofossils, suggesting an intensification of marine primary productivity. Meanwhile, the Tarim Basin may have encountered episodic bottom water deoxygenation supported by an increase in the enrichment factor of redox–sensitive elements such as U and V. The integrated geochemical proxy records suggest that the eastern Tethys has encountered profound ecosystem stress imposed by elevated nutrient fluxes and ocean deoxygenation, which may have been amplified by simultaneously intensified chemical and physical weathering during the PETM.

1. Introduction

The Paleocene–Eocene Thermal Maximum (PETM; ~56 Ma) represents one of the most pronounced carbon cycle perturbation events in the Cenozoic (Gutjahr et al., 2017; Zeebe et al., 2016), characterized by the release of vast amount of carbon dioxide (CO_2) and global warming of 5–9 °C (Dunkley Jones et al., 2013; Frieling et al., 2017; Jones et al., 2013; Tierney et al., 2022; Zhu et al., 2019). The large CO_2 emission is supported by a global negative carbon isotope excursion (CIE) in both terrestrial and marine sedimentary records, with a magnitude of approximately 3 to 6‰ (Jones et al., 2019; McInerney and Wing, 2011). However, the duration, source, rate, and amount of the emitted CO_2 remain controversial (Cui et al., 2011; Gutjahr et al., 2017; Kirtland Turner et al., 2017; Zeebe et al., 2016). Generally, the CIE is associated with an onset of <10 kyr (Zachos et al., 2005), a plateau lasting ~110 kyr (Murphy et al., 2010), and a recovery phase spanning from ~40 kyr (Aziz et al., 2008) to ~80 kyr (Murphy et al., 2010). Various potential sources of emitted CO_2 have been proposed, including destabilization of methane hydrates (Dickens et al., 1995; Katz et al., 2001; Matsumoto, 1995), oxidation of organic matter triggered by the dessication of epicontinental seaway (Higgins and Schrag, 2006), decomposition of organic matter from permafrost (DeConto et al., 2012), wildfires on peatlands (Kurtz et al., 2003), and volcanic CO_2 and thermogenic methane associated with the emplacement of the North Atlantic Igneous

* Corresponding authors.
E-mail addresses: wut1@montclair.edu (Q. Wu), cuiy@montclair.edu (Y. Cui).

https://doi.org/10.1016/j.palaeo.2023.111969
Received 30 June 2023; Received in revised form 8 December 2023; Accepted 11 December 2023
Available online 15 December 2023

Province (NAIP) (Frieling et al., 2016; Storey et al., 2007; Svensen et al., 2010). Chemical weathering of silicate rocks (Colbourn et al., 2015; Pogge von Strandmann et al., 2021) and organic carbon burial (Bowen, 2013; Bowen and Zachos, 2010) are thought to be the mechanisms that drove the PETM recovery. As a result of intensified terrestrial input triggered by enhanced chemical weathering, deoxygenation is widely observed based on sulfur isotopes (Yao et al., 2018), iodine concentrations (Zhou et al., 2014), and trace element geochemistry (Dickson et al., 2014). Regional occurrences of anoxia to euxinia have been found in semi–enclosed shelf regions, such as the Peri–Tethys (Dickson et al., 2014), the North Sea (Schoon et al., 2015), and the Arctic Ocean (Sluijs et al., 2006).

Despite decades of research from multiple locations to understand the causes and consequences of the climatic changes that occurred during the PETM, the eastern Tethys region remains understudied. Recent work on calcareous nannofossil biostratigraphy and stable isotopes support a well-preserved PETM interval at the Kuzigongsu (KZGS) section, Tarim Basin, northwestern China (Wang et al., 2022). To elucidate the environmental changes occurred in the eastern Tethys during the PETM, we collect major, trace, and rare earth element data, as well as clay mineralogy from the study site. These integrated datasets reveal changes in chemical weathering, redox conditions, and marine productivity across the PETM interval. A better understanding of the climatic and environmental responses to rapid CO_2 forcing in the eastern Tethys, an important yet inadequately studied location concerning heat and moisture transport, as well as organic carbon burial, holds crucial implications for anthropogenic climate changes.

2. Geological background

2.1. Regional geology

The Tarim sedimentary basin is located in the west of Xinjiang Uygur Autonomous Region in northwestern China (Fig. 1a), with an elevation of 1.2 km, a length of ~1500 km, and a width of ~700 km. The Tarim Basin is regarded as a repository of the geological history of the Asian continent due to sedimentation since the Paleozoic (Bosboom et al., 2014). During the Paleozoic Era, the Tarim Basin was occupied by marine calcareous and terrigenous deposits until the Carboniferous (Wang et al., 2012), followed by a transition to continental deposition during the Permian Period, extending into most of the Mesozoic sedimentary rocks (Wang et al., 2012). The deformation of coarse–grained clastics during the Mesozoic was triggered by the continuous terrane accretion and ended by the India-Asia collision (Xiao et al., 2004; Yin and Harrison, 2000). From the late Cretaceous to the Eocene, the western Tarim Basin witnessed five marine transgressions and regressions of the

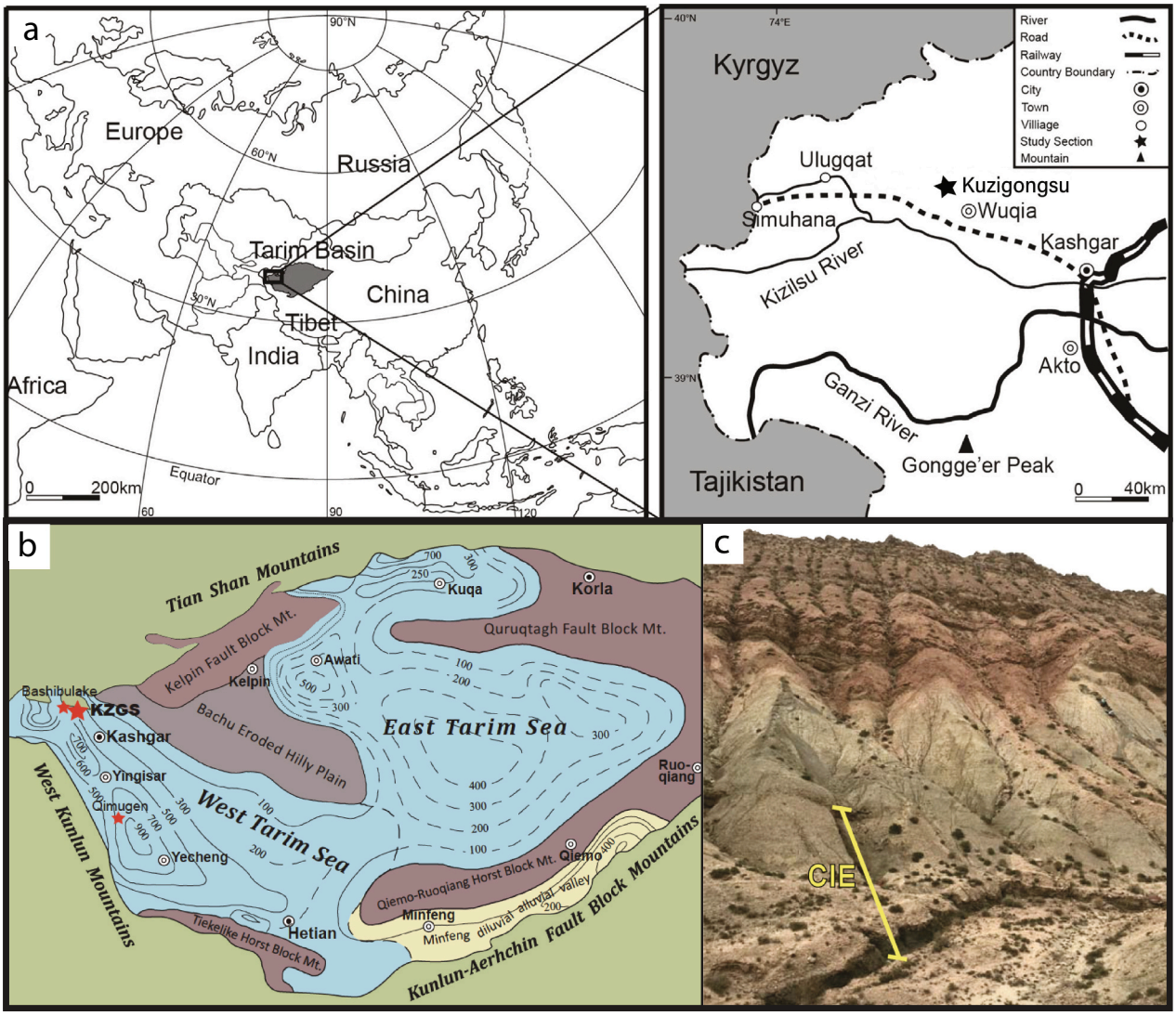

Fig. 1. (a) Location of the Kuzigongsu section (KZGS) in the Tarim Basin, SW China (modified from Cao et al., 2018); (b) Paleobathymetric map of the study site during the early Eocene; (c) Outcrop of the Paleocene–Eocene sequence and the CIE interval is highlighted.

epicontinental sea (Xi et al., 2016; Zhang et al., 2018). By the late Paleocene, the region transformed into a warm semi–restricted seaway that connected the eastern Tethys Ocean and the western Mediterranean Tethys, covering an area of 56,000 km^2 (Cao et al., 2018). The northward movement of the Indian subcontinent into Eurasia from the Cenozoic to the present subjected the Tarim Basin to overthrusting along the margins by the Kunlun Mountains to the south, the Tianshan Mountains to the north (Fig. 1b), and the Pamir Mountains to the west (Yin and Harrison, 2000). Accordingly, the Paleogene marine sequence, known as the Kashi Group (Aertashi, Qimugen, Kalatar, Wulagen, and Bashibulake Formations) is composed of gypsum, limestone, sandstone, and mudstone due to marine incursions, and was terminated by continental sedimentation (Wuqia Group) throughout the basin by the end of the Eocene (Bosboom et al., 2014; Bosboom et al., 2011; Zhang et al., 2018).

Our study site, the Kuzigongsu (KZGS) section (39°45′10″ N, 75°17′29″ E) is situated 5 km northwest of Wuqia county. It comprises approximately 48 m-thick fine-grained sediments of the Qimugen Formation with a change in lithology during the recovery phase of the PETM observed at the outcrop, which may indicate a truncation (Wang et al., 2022). Within the lower part of the Qimugen Formation at the KZGS section, the predominant lithologies are characterized by gray limestones (0–4.1 m and 47.1–47.7 m), gray–greenish calcareous mudstones (4.1–5.8 m, 9.1–29.8 m, 31.2–36.8 m, and 41.2–44.6 m), gray marlstones (5.8–9.1 m, 36.8–41.2 m, and 44.6–47.1 m), with an intercalated layer of bivalve–rich bioclastic limestone (29.8–31.2 m) (Fig. 1c). Previous studies have documented the presence of bivalves (oysters) and large foraminifera within the study section, and calcareous nannofossil biostratigraphy suggests the occurrence of biozones ranging from NP6 to NP10 (Wang et al., 2022; Jiang et al., 2023).

2.2. Nannofossil biostratigraphy

Detailed calcareous nannofossil biostratigraphy was conducted by using a total of 123 specimens with an average of ~0.4 m sampling space (Wang et al., 2022), which recognized nannofossil Zone NP6 through Zone NP10 based on the successive occurrence of five nannofossil datums, thereby affirming the completeness of the PETM in the study section (Wang et al., 2022). Specifically, the base of NP6, the NP7–NP8 boundary, the Zone NP9, the NP9b–NP9a boundary, and the base of NP10 were precisely determined based on the first occurrences of *Heliolithus kleinpellii*, *Heliolithus riedelii*, *Discoaster multiradiatus*, *Discoaster araneus*, and *Rhomboaster bramlettei*, respectively.

2.3. Stable carbon isotope stratigraphy

Negative carbon isotope excursion in marine carbonates supports the occurrence of PETM in the study section (Wang et al., 2022). The carbon isotopes of bulk carbonates ($\delta^{13}C_{carb}$) range from −5.2‰ to 4.7‰ through the entire study section (Fig. 2). The magnitude of $\delta^{13}C_{carb}$ excursion is 6.3‰ (from a pre-PETM average of 1.1‰ to a minimum of −5.2‰) during the PETM, which is followed by a rapid recovery at ~30.5 m. Based on the negative excursion of $\delta^{13}C_{carb}$, we divide the stratigraphic record into pre-PETM (0–19.9 m), PETM (19.9–30.5 m), and post-PETM (30.5–47.6 m) intervals to facilitate the discussion of our geochemical records following Wang et al. (2022). The targeted PETM

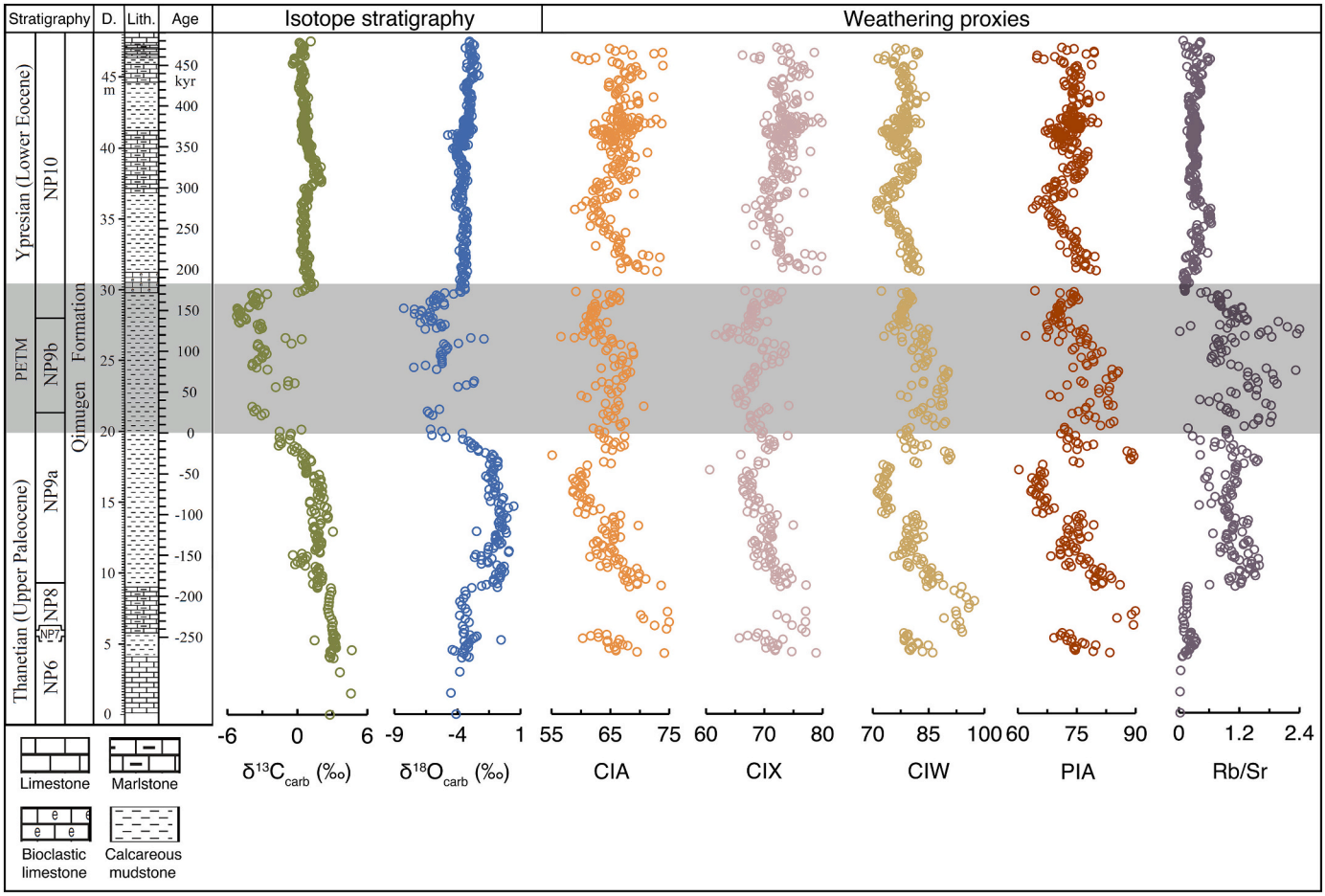

Fig. 2. The stratigraphy and lithology profiles of the Kuzigongsu section. Distributions of carbon ($\delta^{13}C_{carb}$), oxygen ($\delta^{18}O_{carb}$) isotopes (Wang et al., 2022), and chemical weathering proxies CIA, CIX, CIW, PIA, and Rb/Sr along with the profile. PETM interval is highlighted in gray shading.

interval (19.9–30.5 m) is further dissected into the CIE onset (19.9–20.6 m), CIE body (20.6–29.8 m), and CIE recovery (29.8–30.5 m) phases, according to published age model (Röhl et al., 2007).

2.4. Occurrence of the PETM

Multiple lines of evidence support the occurrence of the PETM at the study site, including 1) a 6.3‰ negative excursion in stable carbon isotopes of marine carbonates (Wang et al., 2022) (Fig. 2); 2) moderately high sedimentation rates (6.5 cm kyr^{-1}) (Wang et al., 2022); and 3) calcareous nannofossil biostratigraphy (Zone NP9 and NP10) with abundant excursion taxa (e.g., *Coccolithus bownii*, *Discoaster araneus*, *D. acutus*, and *Rhomboaster bramlettei*) (Wang et al., 2022). The temporal resolution of our PETM records is higher than many deep–sea sites and a recent study in the Tarim Basin (Cao et al., 2018). Specifically, the study site represents a shallow marine environment supported by the occurrence of two characteristic nannofossil species, *Micrantholithus astrum* and *M. flos*, which are indicative of a shallow epicontinental sea (Wang et al., 2022). This is further corroborated by a recent study that identified the Tethys seaway in the southwestern Tarim Basin as a carbonate platform based on the abundant foraminifera and bivalve bioclasts (Wei et al., 2021; Jiang et al., 2023). Spectral analysis using magnetic susceptibility suggests an increase in sedimentation rates associated with sea level rise in the PETM interval (Fig. 3c) (Jiang et al., 2023), which is likely the result of higher terrestrial surface runoff associated with a more rigorous hydrological cycle.

3. Materials and methods

3.1. Major and trace elements analyses

A total of 480 rock samples with an average interval of 10 cm were collected from the study site and ground into powder using the 8000D Mixer/Mill® for geochemical analysis. Major, trace and rare earth elements (REEs = La, Ce, Pr, Nd, Sm, Eu, Gd, Tb, Dy, Ho, Er, Tm, Yb, Lu) were analyzed using the iCAP Q Inductively Coupled Plasma – Mass Spectrometry (ICP–MS) located at the Department of Earth and Environmental Studies in Montclair State University. After each sample was ground and homogenized, around 0.1 g (±0.0005 g) of powder was mixed with 0.4 g (±0.002 g) of lithium metaborate from Spex® CertiPrep and fused at 1050 °C for 40 min in the Thermo Scientific™ Lindberg/Blue M™ Moldatherm™ Box Furnace. Subsequently, melted samples were dissolved in 50 mL of 7% HNO_3 (dilution factor of 500×), and then processed to the second dilution using 0.5 mL "mother" solution and 9.5 mL of 2% HNO_3 (dilution factor of ~10,000× in total) before ICP–MS analysis. The reported results are calibrated with eight standards from the U.S. Geological Survey (AGV–2, BCR–2, BHVO–2, BIR–1, DNC–1, G–2, GSP–2, and W–2), and are averaged with three analytical runs for each sample. The analytical precision (1σ) for all elements is better than 10%. Instrument drift (less than ±2% over the 2-

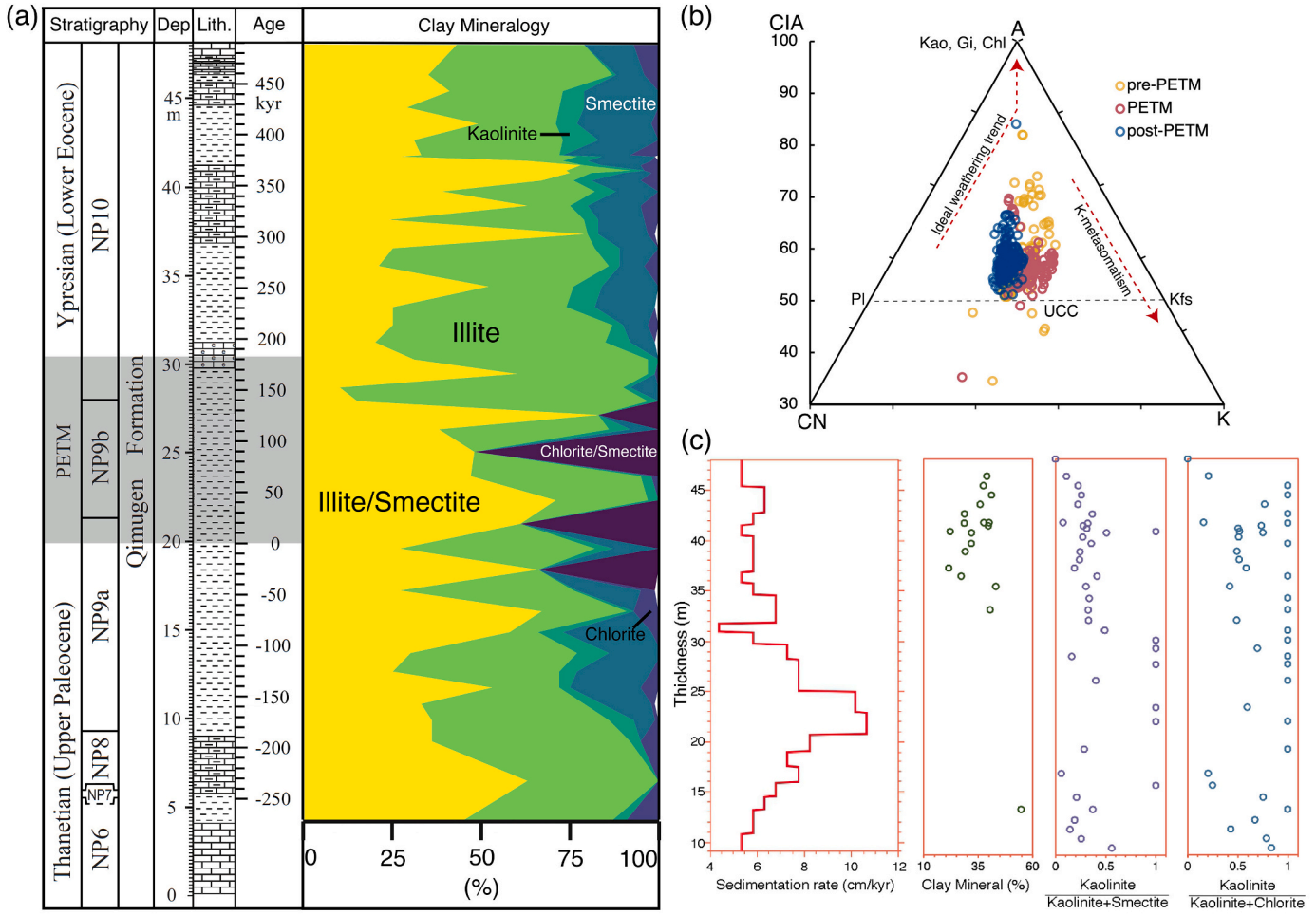

Fig. 3. (a) Normalized abundance (wt%) among clay minerals; (b) Ternary diagram of A–CN–K of the Kuzigongsu section. A = Al_2O_3, CN = CaO* + Na_2O, K = K_2O, Kao = kaolinite, Gi = gibbsite, Chl = chlorite, Pl = plagioclase, Kfs = K–feldspar, UCC = Upper Continental Crust; (c) Sedimentation rate, relative abundance of clay mineral in the bulk rock (%), kaolinite-smectite ratio (computed as kaolinite/(kaolinite+smectite)), and kaolinite-chlorite ratio (computed as kaolinite/(kaolinite+chlorite)) at the KZGS section.

to 3-h run) was corrected by analyzing a matrix–matched drift monitor that was regularly spaced throughout each analytical run.

Using the major element concentration data obtained from the ICP–MS analysis, chemical weathering indices, including Chemical Index of Alteration (CIA), modified Chemical Index of Alteration (CIX), Chemical Index of Weathering (CIW), and Plagioclase Index of Alteration (PIA) are calculated. The CIA ($[Al_2O_3 / (Al_2O_3 + CaO^* + Na_2O + K_2O) \times 100]$) is used to quantify the degree of feldspar transformed into clay minerals during chemical weathering processes (Nesbitt and Young, 1982), where CaO* refers to the CaO fraction in the silicates rather than that in carbonates or phosphates (Fedo et al., 1995) and is calculated as the minimum value of ($CaO - P_2O_5 \times 10/3$) and Na_2O (McLennan, 1994; Panahi et al., 2000). The difference between CIX ($[Al_2O_3 / (Al_2O_3 + Na_2O + K_2O) \times 100]$) and CIA is the omission of CaO* (Garzanti et al., 2014), which allows for assessing the weathering condition of sedimentary rocks that contain detrital or authigenic carbonates (e.g., bioclasts). The CIW ($[Al_2O_3 / (Al_2O_3 + CaO^* + Na_2O) \times 100]$) was proposed to exclude the potassium reintroduction during post-diagenesis process (Harnois, 1988), while PIA ($[(Al_2O_3 - K_2O) / (Al_2O_3 + CaO^* + Na_2O - K_2O)] \times 100$) tracks the degree of plagioclase weathering (Fedo et al., 1995). Because these weathering proxies are most useful for siliciclastic sediments (Fu et al., 2023; Zhao and Zheng, 2015), we only discuss data from marlstone and calcareous mudstone for chemical weathering analysis to better interpret depositional processes.

Enrichment factors (EF) relative to average shales of provenance-, paleoproductivity-, and redox-sensitive elements are calculated to track changes in provenance (Ti_{EF}, Zr_{EF}, and Cr_{EF}), paleoproductivity (P_{EF}, Ba_{EF}, Ni_{EF}, and Cu_{EF}), and redox conditions (U_{EF} and V_{EF}) (Chaillou et al., 2002; McManus et al., 2005; Takahashi et al., 2014; Tribovillard et al., 2006). We normalize the concentration of trace elements to aluminum (Al) content, which represents detrital fraction in aluminosilicate phases that are relatively stable during diagenesis (Calvert and Pedersen, 1993; Tribovillard et al., 2006). Therefore, EF of selected elements (Ti, Zr, Cr, P, Ba, Ni, Cu, U, and V) were calculated as $X_{EF} = [(X/Al)_{sample} / (X/Al)_{average\ shale}]$ (Wedepohl, 1971, 1991) to describe the enrichment degree of the environmentally sensitive elements relative to average shales (Wedepohl, 1971, 1991). Additionally, all measured concentrations of REEs were normalized to the Post–Archean Australian Shale (PAAS) (Pourmand et al., 2012). Cerium (Ce) anomalies were calculated as $Ce/Ce^* = (2 \times Ce_{SN}) / (La_{SN} + Pr_{SN})$, where SN stands for PAAS normalized value (Ce–88.25, La–44.56, and Pr–10.15) (Bau et al., 1996).

3.2. Clay minerals

48 bulk rock samples with ~1 m interval and > 10 g weight were analyzed by X–ray diffraction (XRD) at the State Key Laboratory of Geological Processes and Mineral Resources, China University of Geosciences (Wuhan), following the procedures presented by Shen et al. (2022). Powdered and homogenized samples were decarbonated with 0.2 M HCl to remove carbonates before concentrating the clay–sized particles using the deflocculation method (Shen et al., 2022). Subsequently, unoriented bulk rock samples and oriented clay aggregates (<2 μm) were analyzed using a PANalytical X'Pert Pro X–ray Diffractometer with CuKα radiations under a 40 kV voltage and a 25 mA intensity. The bulk rock samples and clay aggregates were air–dried and analyzed for clay mineral X–ray diffraction peaks. Two additional runs for clay aggregates in 2 h–heating at 490 °C were performed subsequently after ethylene–glycol saturation (Moore and Reynolds Jr, 1989). The identification and quantification of bulk minerals generally relied on the examination of specific diffraction peaks: quartz (4.26 Å), K–feldspar (3.24–3.25 Å), plagioclase (3.18–3.20 Å), hematite (2.69 Å) and calcite (3.02 Å). Clay minerals were identified through distinctive peak series and shifts observed among the three measurements for each sample described above. For example, illite was diagnosed by the (10 Å, 5 Å, 3.33 Å) peak series continuously after each of the three steps mentioned above; chlorite was characterized by the peak series (14.2 Å, 7.1 Å, 4.7 Å, 3.54 Å) and nearly vanished after the 2 h–heating treatment; illite–smectite mixed layer (I/S) was recognized by 11–14 Å peak after air–drying, moved towards smaller peak after ethylene–glycol immersion, and dropped to 10 Å after heating; and kaolinite was represented by both the 7.18 Å and 3.58 Å peaks (Shen et al., 2022).

4. Results

4.1. Major elements

The Qimugen Formation at the study section is composed of SiO_2 (12.2–74.6%), Al_2O_3 (5.4–30.6%), Fe_2O_3 (0.9–22.1%), CaO (0.2–87.5%), MgO (0.2–7.8%), K_2O (0.2–10.8%), Na_2O (0.02–7.1%), and a small amount of TiO_2 (<3.5%), P_2O_5 (<2.4%), and MnO (<0.5%) (Supplementary Data). At the CIE onset, the content of most oxides remains relatively stable, with the exception that K_2O content decreases from 6.5% to 1.5% in the middle of the CIE body (~24 m). The content of SiO_2 and CaO decreases abruptly (58% to 32% for SiO_2, and 52% to 22% for CaO) during the CIE recovery phase. Weathering proxies (CIW & PIA) show a noticeable increase at the beginning of PETM (80% to 90% for CIW, and 72% to 86% for PIA), whereas the Rb/Sr ratio starts to increase from 0.2 to 1.4 at ~8 m and reaches its maximum value of 2.4 during the PETM (Fig. 2). Remarkably, all major elements–related indices (CIA, CIX, CIW, and PIA) display moderate increases in the later part of the PETM interval (at ~27 m) and the beginning of the post-PETM interval (at ~29.8 m).

4.2. Clay mineralogy

The dominant clay minerals at the study site are illite (0%–82%, average 36%) and mixed illite/smectite (I/S; 10%–83%, average 44%) with subordinate smectite (0%–25%, average 10%) (Fig. 3a). The clay mineral assemblage also features a small percentage of kaolinite (0%–10%, average 4%) and chlorite (0%–9%, average 2%) throughout the section, and two small increases in kaolinite abundance in the post-PETM interval (at ~31 m and ~42 m). The abundance of illite/smectite mixed layers increases from 27% to 61% at the CIE onset (Fig. 3a; Table 1). Illite becomes more abundant (from 25% to 80%) in the CIE body (at ~28 m). Additionally, kaolinite exhibits a modest increase from 1% to 10% in the post-PETM interval (at ~42 m). Overall, the content of bulk clay minerals increases from 27% at ~36 m to 39% at ~46 m following the PETM, which coincides with the higher ratios of kaolinite/(kaolinite+smectite) and kaolinite/(kaolinite+chlorite) (Fig. 3c).

4.3. Enrichment factors of trace elements and REEs

4.3.1. Provenance proxies

Provenance proxies exhibit consistently low values throughout the entire section (average values of Ti_{EF}, Zr_{EF}, and Cr_{EF} are 1.0, 1.3, and 1.3, respectively), with a Zr_{EF} peak and a decrease in Cr_{EF} from 1.76 to 0.85 in the post-PETM interval (Fig. 4). Furthermore, Er_{SN}/Tm_{SN} ratios remain relatively stable (~ 1) in the PETM interval, with a small increase to near 1.2 at 41.6 m in the post-PETM interval. The PETM

Table 1
Average percentage of each clay mineral and mixed layer within pre-PETM, PETM, and post-PETM intervals.

Interval	Smectite	Illite	Chlorite	Kaolinite	Illite/Smectite	Chlorite/Smectite
pre-PETM	10%	37%	3%	4%	43%	3%
PETM	2%	39%	0%	2%	46%	11%
post-PETM	13%	35%	2%	5%	44%	0%

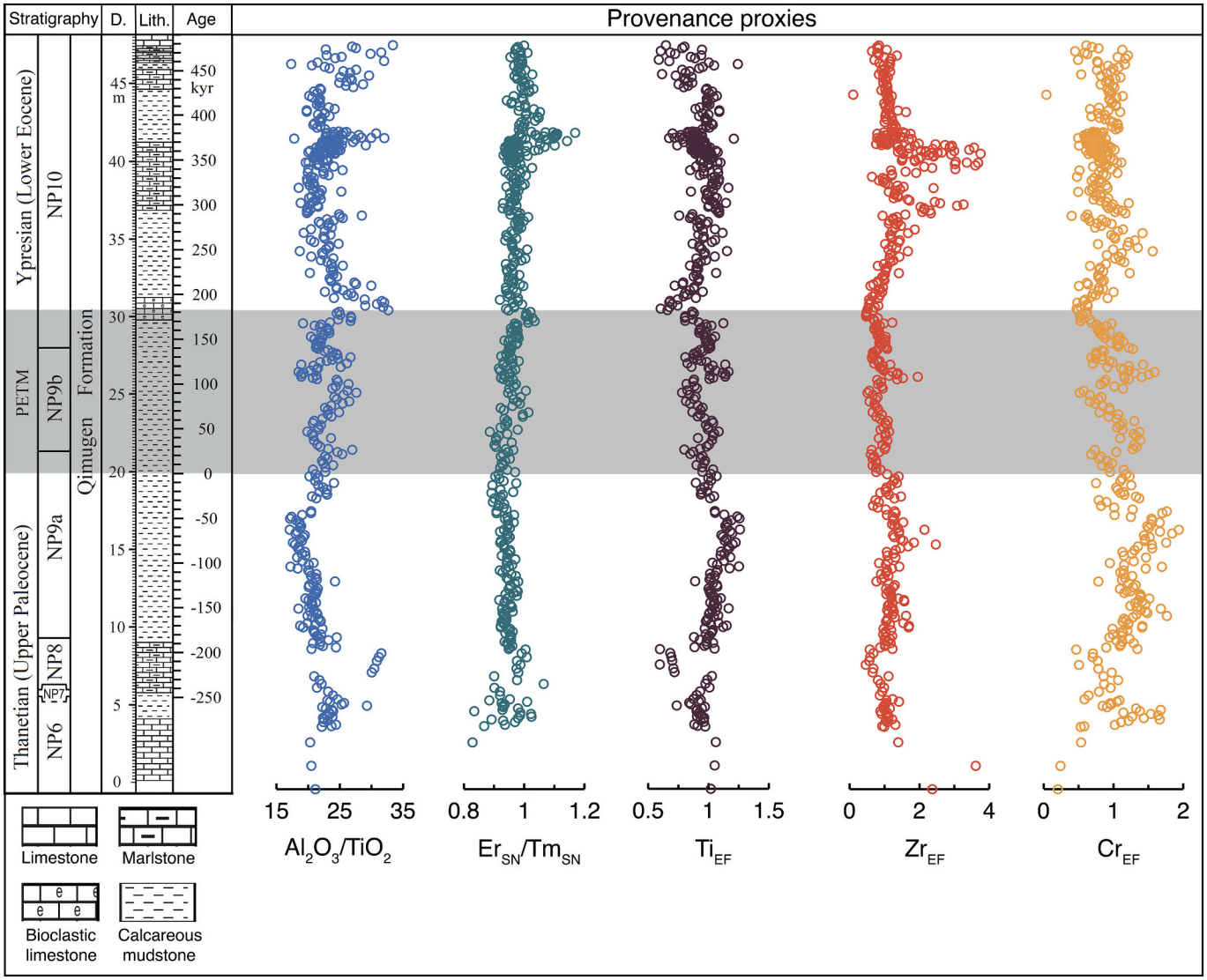

Fig. 4. Stratigraphic distribution of provenance proxies Al_2O_3/TiO_2, Er_{SN}/Tm_{SN}, Ti_{EF}, Zr_{EF}, and Cr_{EF}.

average and the post-PETM average Er_{SN}/Tm_{SN} values are statistically different at 95% significance level based on Welch's t–test ("t.test" function in R statistical software) (Fig. 4). The pattern of PAAS–normalized REEs serves as another proxy for sediment provenance (Fig. 5a) (McLennan et al., 1993). The REEs is dominated by Tb in the pre-PETM interval, which is then switched to Eu in the PETM interval. Additionally, the abundance of REEs of each sample is more variable during the PETM compared to that in the pre- and post-PETM intervals (Fig. 5a).

4.3.2. Marine paleoproductivity and redox proxies

Notably, paleoproductivity proxies (Ba_{EF}, Ni_{EF}, and Cu_{EF}) and redox proxies (U_{EF} and V_{EF}) display an overall increasing trend with pronounced and concurrent oscillations within the PETM interval. As a paleoproductivity proxy, Cu_{EF}, exhibits a large increase from approximately 0.5 to 2 during the PETM, suggesting significant inputs of Cu into the depositional site. In contrast, P_{EF} displays an average value of 2.0 in the lower part of the study section, fluctuates around 0.9 during the PETM, and reaches 2.1 at 41.6 m in the post-PETM interval (Fig. 6). Ni_{EF} is averaged at 0.6, and exhibits an increase to 1.6 at approximately 27 m in the post-PETM interval. Redox proxies U_{EF} and V_{EF} both show increasing trend during the PETM, reaching their maximum value of 8.25 at 27.1 m and 2.94 at 21.9 m, respectively. The Ce anomaly fluctuates around 1.0, with a minimum of 0.8 observed at 9 m in the pre-PETM interval, and remains relatively stable in both PETM and post-PETM intervals.

5. Discussion

5.1. Changes in weathering and sediment provenance across the PETM

Weathering intensity is expected to increase as a result of elevated CO_2 levels, rising temperatures, and enhanced hydrological cycles during the PETM (Gislason et al., 2009; Li et al., 2016; Tanaka et al., 2022; West et al., 2005). Several lines of evidence support increased silicate weathering during the PETM, including increased silica–rich sedimentary deposits in North Atlantic (Penman, 2016), higher chemical index of weathering in central China (Chen et al., 2016), elevated clay abundance (primarily kaolinite) in Svalbard (Dypvik et al., 2011), increased flux of radiogenic Os in the Arctic Ocean and Peri–Tethys (Dickson et al., 2015), and negative shifts in lithium isotopes of marine carbonates and shales in Pacific and North Atlantic (Pogge von Strandmann et al., 2021). Here we aim to reconstruct changes in weathering across the PETM using a number of weathering proxies, including CIA, CIX, CIW, PIA, and Rb/Sr ratios (see Materials and Methods for how to calculate these proxies), and assess whether changes in sediment provenance

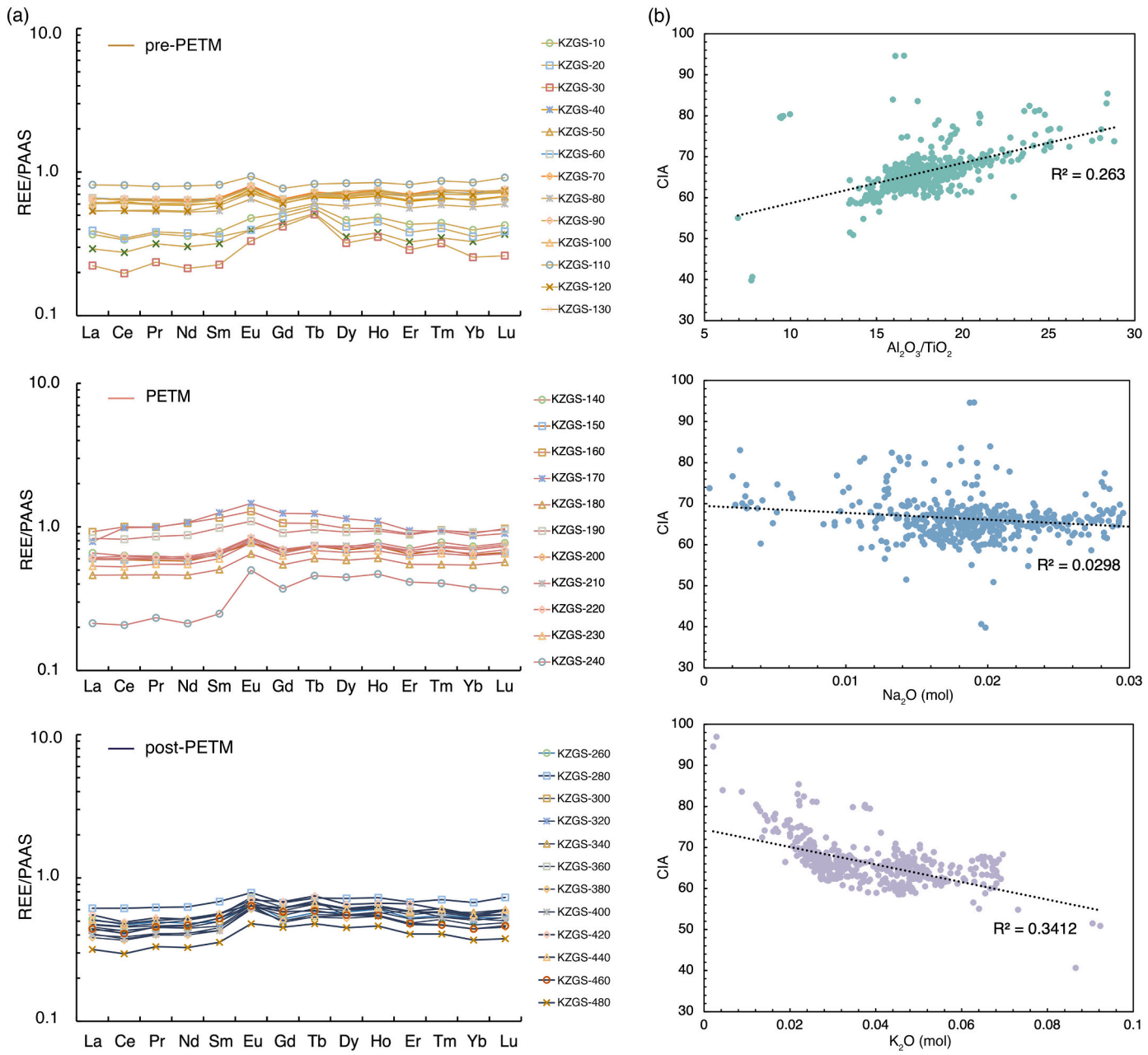

Fig. 5. (a) REEs patterns of ~2 m–spaced samples divided into pre–PETM, PETM, and post–PETM intervals; (b) Cross-plots of CIA and Al_2O_3/TiO_2, Na_2O, and K_2O, respectively.

impact the proxy–based interpretation of weathering at the study site. Enhanced weathering in the eastern Tethys is supported by a significant increase in Rb/Sr ratios, major element–based weathering proxies, and illite abundance (Fig. 2 and Fig. 3a).

5.1.1. Chemical weathering indices

Major element–based geochemical weathering indices (CIA, CIX, CIW, and PIA) have been widely used as indicators of chemical weathering in siliciclastic sediments due to preferential leaching of soluble elements such as Ca, Na, Mg, and K from feldspars, leaving refractory elements like Al, Fe, and Ti retained in weathering products (Fedo et al., 1995; Nesbitt and Young, 1982). Increased global temperature and more rigorous hydrological cycle can lead to intensified reaction between carbonic acid and silicates, which releases more dissolved cations (such as K^+, Ca^{2+}, and Mg^{2+}) and alkalinity (e.g., bicarbonate and carbonate ions) into the ocean, leading to depletion of mobile elements (K, Ca, Mg and Na) relative to immobile elements (e.g., Al) and increased values of chemical weathering indices (McLennan, 1993). Higher values of chemical weathering indices (e.g., CIA) have been observed in North Sea (Stokke et al., 2020), Svalbard (Wieczorek et al., 2013), central China (Chen et al., 2016), and northern Peri–Tethys (Dickson et al., 2014) during the PETM. At our study site, enhanced chemical weathering is supported by increased values of CIA, CIW, and PIA during the onset and body of the PETM. These observations are consistent with warming–induced increase in chemical weathering during the PETM.

The inferred enhanced chemical weathering is further corroborated by a significant increase in Rb/Sr ratios in the PETM interval at the study site. Rb/Sr ratio is another useful proxy for clay mineral weathering because of different geochemical behaviors of Rb and Sr during chemical weathering (Chen et al., 1999; Dasch, 1969). For example, the Ca—Sr pair in Ca–bearing minerals (e.g., hornblende, plagioclase, and picrite) can be leached out much easier compared to the K—Rb pair in the K–rich

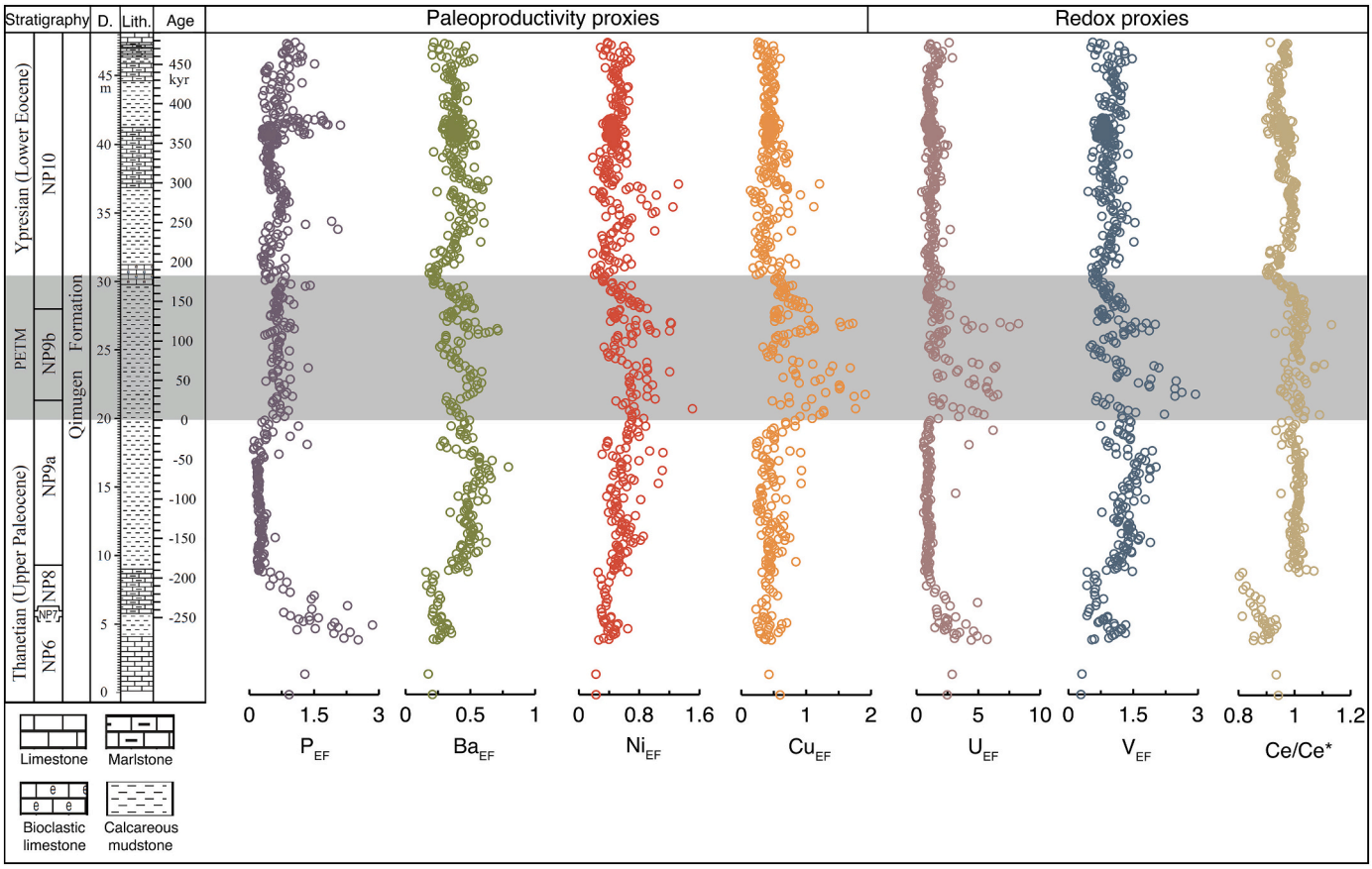

Fig. 6. Stratigraphic distribution of paleoproductivity proxies P_{EF}, Ba_{EF}, Ni_{EF}, and Cu_{EF}, along with redox conditions proxies U_{EF}, V_{EF}, and Ce/Ce*.

minerals (e.g., K–feldspar, biotite), such that the residue is depleted in Ca—Sr but enriched in K—Rb, leading to an increase in Rb/Sr ratio during intense chemical weathering (McLennan et al., 1993; Perri, 2018; Xu et al., 2010). The increase in Rb/Sr ratios at our study site is supportive of enhanced chemical weathering. Additionally, increased Rb/Sr ratios have been observed in India and Svalbard across the Paleocene–Eocene transition (Rahi et al., 2022; Schlegel et al., 2013), indicating global extent of enhanced chemical weathering.

5.1.2. A–CN–K diagram

In addition to the depth profiles of chemical weathering indices, the Al_2O_3–(CaO* + Na_2O)–K_2O (A–CN–K) ternary diagram is a valuable tool to assess the original composition of the source rocks and to evaluate the extent to which samples are impacted by K–metasomatism (Fedo et al., 1995; Nesbitt et al., 1992; Panahi et al., 2000). Previous studies reveal a leaching sequence dominated by plagioclase and K–feldspar during the weathering of the upper continental crust (UCC), which is characterized by an initial depletion of Na_2O, CaO, and K_2O in the early stage of weathering, followed by the loss of K_2O and formation of kaolinite or gibbsite in more advanced stages of weathering (Panahi et al., 2000). As a result, an ideal weathering trend is subparallel to the A–CN axis towards the A apex as weathering progresses for samples with the same source materials (Fedo et al., 1995). The data from the PETM and pre- and post-PETM intervals at our study site exhibit similar pattern on an A–CN–K diagram, which supports stable source materials (Fig. 3b). Moreover, K–metasomatism, a post–burial alteration process that usually occurs during illitization or authigenic formation of K–feldspars (Panahi et al., 2000), may induce deviations from the ideal weathering trend towards the K apex. Since we did not observe any obvious shift in trend towards K–apex in our A–CN–K diagram at our study site, we suggest that K–metasomatism did not play a significant role. However, we cannot completely exclude the K–addition in the PETM interval, because an increased illite content may be the result of conversion of smectite to illite during enhanced chemical and physical weathering processes due to increased pCO_2 and temperature during the PETM (Meunier et al., 2004; Pogge von Strandmann et al., 2021) (Fig. 3a, b).

5.1.3. Hydrological cycle

In addition to rising pCO_2 and temperature, intensified hydrological cycle would have further enhanced physical and chemical weathering during the PETM (Camuffo, 1995; Kump et al., 2000; Pagani et al., 2006; Sluijs et al., 2011). Increased precipitation and surface run–off in the eastern Tethys is supported by a significant increase in the abundance of bulk clay mineral and two notable peaks in kaolinite abundance in the post-PETM interval, corroborating a more dynamic global hydrological cycle at this time (Carmichael et al., 2017; Carmichael et al., 2016; John et al., 2012; Tateo, 2020). This may also indicate increased physical erosion (Chamley, 2013; Colin et al., 1999; Deconinck et al., 2019), in addition to enhanced chemical weathering, as a result of intensified seasonal precipitation and surface runoff at middle to high latitudes (Foreman et al., 2012; Jiang et al., 2021; Schmitz and Pujalte, 2007). In addition, climate model simulations suggest that the tropical and subtropical regions may have experienced episodic but intense precipitation on land (Carmichael et al., 2018; Kiehl and Shields, 2013; Shields et al., 2021), which is consistent with the intensification of physical erosion in mid– to low–latitudes, demonstrated by increased mass accumulation rates of petrogenic organic carbon (OC_{petro}) (Lyons et al., 2019). The overall low kaolinite content in the PETM interval at our study site in the subtropics (Fig. 3a) differs from the increased kaolinite contents at other mid– and high–latitudinal sites (Dypvik et al., 2011; Gibson et al., 2000; Robert and Kennett, 1994; Stokke et al., 2020), which may be the result of strong physical erosion associated with episodic and intense

precipitation. The interpreted increase in precipitation in the eastern Tethys, however, is in contrast to the results of paleoclimate data assimilation (DA) and Deep–Time Model Intercomparison Project (DeepMIP) that show a decrease in *P E* (Precipitation minus Evaporation) associated with enhanced evaporation near the study site (Cramwinckel et al., 2023; Tierney et al., 2022), suggesting that there is a clear need to obtain more detailed hydrological records and refine Earth system model to match the interpreted hydrological changes in this important region that regulates heat and moisture transport during a major global climate change.

5.1.4. Impact of potential changes in sediment provenance on proxy–based interpretation of weathering

Provenance indicators suggest that the sediment provenance remains relatively stable across the PETM interval with minor changes. The small variation of Al_2O_3/TiO_2 ratios (varying between 18.5 and 27.6) suggests a relatively stable sediment source during the PETM (Fig. 4), as they are immobile during weathering and reflective of source rock components (Hayashi et al., 1997; Nesbitt and Young, 1982; Panahi et al., 2000). This is further supported by stable Zr_{EF} values around 1.0 in the PETM interval (Fig. 4), because Zr is an immobile element primarily associated with heavy minerals and mainly affected by the behaviors of source rocks rather than climatic changes (Scheffler et al., 2006; Zhou et al., 2015). Similarly, Ti and Cr are also immobile and occur in heavy minerals during chemical weathering (Hayashi et al., 1997), which remain relatively invariant, supporting no significant change in source materials during the PETM. We note that CIA is weakly correlated with the the provenance indicators (Al_2O_3/TiO_2) ($R^2 = 0.263$; *p*–value <0.0001; Fig. 5b) and K_2O ($R^2 = 0.341$; *p*–value <0.0001; Fig. 5b), but nearly non-correlated with Na_2O ($R^2 = 0.030$; *p*–value <0.0001; Fig. 5b), suggesting the chemical indices of weathering may have been slightly influenced by provenance changes during the PETM. Additionally, a recent study by Fu et al. (2023) suggests that the interpretation of the weathering proxies (e.g., CIA and CIW) can be biased by other factors such as hydrodynamic sorting during transport and deposition, sediment recycling, and diagenesis during post–burial processes (Fu et al., 2023; Garzanti and Resentini, 2016; Guo et al., 2018). Despite these factors that may complicate the major-element based weathering proxies, the higher Rb/Sr ratio provides another independent line of evidence for increased chemical weathering during the PETM.

The distribution patterns of REEs support minor changes in sediment provenance across the PETM (Fig. 5a). Because the bulk rocks are not strongly influenced by diagenetic, metamorphic and other alteration processes, the REEs should have preserved the source rocks' characteristics (Mclennan, 2018; Zimmermann and Bahlburg, 2003). The transition of the dominant element from Tb to Eu starting within the pre-PETM interval may be attributed to changes in the source rock. As the most inert elements among the REEs, Er_{SN}/Tm_{SN} ratios remain invariable over the pre-PETM and PETM intervals (McLennan, 1994). While most PAAS–normalized REEs values are <1.0 at the study site, values higher than 1.0 occur exclusively within the PETM interval, suggesting an additional source into the sediment provenance. Accordingly, we consider the effects of provenance change on Al_2O_3/TiO_2, Ti_{EF}, Zr_{EF}, and Cr_{EF} to be small, and variation in REEs may have been attributed to slight source changes across the PETM.

5.2. Changes in marine productivity across the PETM

It is widely recognized that intensified marine primary productivity may have been triggered by increased inputs of bio-essential elements, such as P, Fe, Cu, and Ni, as a consequence of enhanced weathering and potential volcanic activities (Schoepfer et al., 2015; Shen et al., 2015). It has been observed that Ba_{EF} and P_{EF} are positively correlated with marine primary productivity, but their abundance is likely influenced by changes in the accumulation rates of organic-matter-rich sediment or bottom water redox conditions (Schoepfer et al., 2015; Tribovillard et al., 2006). Additionally, Ni_{EF}, and Cu_{EF} are useful proxies for paleoproductivity because Ni and Cu serve as important micronutrients in organometallic complex (Horner et al., 2021; Tribovillard et al., 2006). The observed increase in both P_{EF} and Ni_{EF} at ~17 m and an abrupt rise in Cu_{EF} at ~18 m at the study site support enhanced nutrient inputs and elevated primary productivity preceding the PETM (Fig. 6). In addition, the widespread occurrence of the calcareous nannoplankton species *Neochiastozygus junctus* during the PETM is indicative of mesotrophic to eutrophic conditions, further supporting an increase in nutrient and primary productivity in the eastern Tethys (Wang et al., 2022). Enhaced primary or export productivity is also observed in the open ocean (Bridgestock et al., 2019; Ma et al., 2014), the continental margin (John et al., 2008; Papadomanolaki et al., 2022), and restricted basin (Sluijs et al., 2008), supporting globally extent of increased productivity during the PETM.

5.3. Changes in marine redox conditions across the PETM

The occurrence of ocean anoxic events (OAE) or expansion of oxygen minimum zones (OMZ) can be attributed to the increased biological productivity and subsequent remineralization of organic matter, which consumes oxygen (Dumitrescu and Brassell, 2005; Reolid et al., 2012; Xiong et al., 2012). The enrichment of redox–sensitive trace elements (e.g., U and V) in marine sediments can be used as a proxy for marine redox conditions as their valences and solubilities vary with redox potential (Chaillou et al., 2002; Takahashi et al., 2014; Tribovillard et al., 2006). For example, in reduced environments, soluble U^{6+} tends to form the insoluble U^{4+} complexes with hydroxides, hydrated fluorides, and phosphates, which can be preserved in the sediments (Andersen et al., 2017; Ivanovich and Harmon, 1992; Morford et al., 2005; Stirling et al., 2007). Unlike the element U, the reduction behavior of V differs under anoxic (non-sulfidic) vs. euxinic conditions, as the presence of H_2S can accelerate the precipitation of trivalent V in the forms of V_2O_3 or $V(OH)_3$ (Algeo and Maynard, 2004). Therefore, episodic increases in U_{EF} and V_{EF} during the PETM at the study site supports a reduced environment and shallow-ocean deoxygenation (Fig. 6).

Additionally, Ce anomaly (Ce/Ce*) is a well–established proxy for reconstructing the redox state of the seawater (Bau and Koschinsky, 2009; Lawrence et al., 2006). The soluble Ce^{3+} is preferentially oxidized to insoluble Ce^{4+} through scavenging by manganese oxyhydroxide under oxic conditions, resulting in a depletion of Ce relative to other neighboring trivalent REEs in the water column, and therefore displaying negative Ce anomalies (Byrne and Sholkovitz, 1996). Hence, the lack of negative Ce/Ce* values in pore waters indicates more reduced conditions of the bottom water (Haley et al., 2004; Zhou et al., 2016). However, dissolution of Mn oxyhydroxide particles under hypoxic–suboxic water conditions may also increase the dissolved Ce content (De Carlo et al., 1997). Therefore, the observed small increase in Ce/Ce* pattern during the PETM may be associated with hypoxic–suboxic water conditions. It is important to note that the anoxia of shallow marine is likely a local phenomenon during the PETM (Gupta and Kumar, 2019; Shukla and Sharma, 2018; Yao et al., 2018), in line with the suggestion that seafloor anoxia expanded <2% during the PETM based on uranium isotope records (Clarkson et al., 2021). Furthermore, intensified ocean stratification is supported by the reduced surface–deep ocean $\delta^{13}C$ gradient (Kwon et al., 2022), i.e., greater CIE magnitudes in shallow marine carbonates compared to those observed in the deep sea (Li et al., 2017; McInerney and Wing, 2011; Self-Trail et al., 2017).

5.4. Relationship between the NAIP activity, silicate weathering, marine productivity, and ocean hypoxia in the eastern Tethys

The emplacement of the North Atlantic Igneous Province (NAIP) is widely considered as the trigger of the PETM (Berndt et al., 2023; Frieling et al., 2016; Gutjahr et al., 2017; Jones et al., 2023; Jones et al., 2019; Svensen et al., 2004). Large emissions of CO_2 from both intrusive

and extrusive NAIP activities and associated warming may have led to the release of 2000 to 14,900 Pg C during the PETM at a rate of 0.3 to 1.1 Pg C yr^{-1} (Cui et al., 2011; Gutjahr et al., 2017; Haynes and Hönisch, 2020; Zeebe et al., 2016; Zeebe et al., 2009). Atmospheric CO_2 emission during the PETM is followed by carbon sequestration through silicate weathering (Penman, 2016) and organic carbon burial (Bowen and Zachos, 2010; Komar and Zeebe, 2017; Papadomanolaki et al., 2022), leading to a rapid CO_2 drawdown. Increased carbon sequestration following the PETM is supported by Os isotopes (Dickson et al., 2015), Li isotopes (Pogge von Strandmann et al., 2021), accumulation of biogenic silica and carbonate in the deep oceans (Penman, 2016), and organic carbon deposition in both terrestrial and marine sediments (Bowen, 2013; John et al., 2008).

During enhanced weathering, increased terrestrial runoff may have prompted an increase in nutrient input, stimulating greater marine productivity and leading to higher export of organic carbon to the seafloor, as evidenced by the increase in P_{EF}, Ni_{EF}, and Cu_{EF} at the study site. The higher total organic carbon content (TOC wt%) and changes in the enrichment of redox-sensitive elements (e.g., U_{EF}, V_{EF} and Ce anomaly) support deoxygenation in the eastern Tethys. This is consistent with a recent suggestion that the Eurasian epicontinental sea played an important role as a carbon sink (720 to 1300 Pg C organic carbon burial; see Kaya et al., 2022) by depositing extensive sapropel during the PETM, which acted as a negative feedback mechanism to draw down atmospheric pCO_2 (Kaya et al., 2022; Papadomanolaki et al., 2022; Yao et al., 2018).

6. Conclusions

Based on the new high–resolution geochemical and clay mineral records from the shallow marine Kuzigongsu section, we reconstructed continental weathering, sedimentary provenance, marine productivity, and ocean deoxygenation of the eastern Tethys during the PETM. Moderate increase in CIW, PIA, and Rb/Sr suggests increased terrestrial input shortly after the PETM onset, possibly due to intensified chemical weathering. Furthermore, illite became more abundant than smectite during the PETM, supporting aggravated physical erosion along with enhanced chemical weathering in altering the composition of major elements. The relatively stable heavy–mineral–associated elements (Ti, Zr, and Er/Tm) and small change in the distribution patterns of REEs imply a minor alteration in sediment provenance, which may be due to volcanic activities. Enhanced nutrient inputs and elevated primary productivity are supported by increases in P_{EF}, Ni_{EF}, and Cu_{EF}. Episodic deoxygenation of seawater is supported by the enrichments of redox–sensitive trace elements (U & V) associated with elevated primary productivity during the PETM. The sub–tropical eastern Tethys site may have provided several key feedbacks to the carbon cycle perturbation, including increased organic carbon burial from higher nutrient inputs and more reduced conditions, and enhanced atmospheric and oceanic circulations to transport warm and moist air and warm water into the northern high latitudes.

CRediT authorship contribution statement

Qingting Wu: Conceptualization, Investigation, Methodology, Writing – original draft, Writing – review & editing, Data curation, Formal analysis, Visualization. **Ying Cui:** Conceptualization, Formal analysis, Funding acquisition, Investigation, Methodology, Project administration, Supervision, Writing – original draft, Writing – review & editing. **Yasu Wang:** Investigation, Writing – review & editing. **Shijun Jiang:** Conceptualization, Funding acquisition, Investigation, Writing – review & editing. **Yixin Dong:** Formal analysis, Visualization, Writing – review & editing. **Jun Shen:** Formal analysis, Methodology, Writing – review & editing, Funding acquisition.

Declaration of Competing Interest

The authors declare no competing interests.

Data availability

The data are made available as a supplementary file

Acknowledgments

We thank Dr. X. Li, A. Gachetti, and M. De Palma for their assistance with ICP–MS analysis. This study was supported by the the National Key R&D Program of China (2022YFF0802900) to J.S., National Science Foundation (2002370, 2026877) to Y.C., the National Natural Science Foundation of China (41888101) and the National Key R&D Program of China (2022YFF0800800) to S.J.. This study is a contribution to IGCP 739.

Appendix A. Supplementary data

Supplementary data to this article can be found online at https://doi.org/10.1016/j.palaeo.2023.111969.

References

Algeo, T.J., Maynard, J.B., 2004. Trace-element behavior and redox facies in core shales of Upper Pennsylvanian Kansas-type cyclothems. Chem. Geol. 206, 289–318.
Andersen, M.B., Stirling, C.H., Weyer, S., 2017. Uranium isotope fractionation. Rev. Mineral. Geochem. 82, 799–850.
Aziz, H.A., Hilgen, F.J., van Luijk, G.M., Sluijs, A., Kraus, M.J., Pares, J.M., Gingerich, P. D., 2008. Astronomical climate control on paleosol stacking patterns in the upper Paleocene–lower Eocene Willwood Formation, Bighorn Basin, Wyoming. Geology 36, 531–534.
Bau, M., Koschinsky, A., 2009. Oxidative scavenging of cerium on hydrous Fe oxide: evidence from the distribution of rare earth elements and yttrium between Fe oxides and Mn oxides in hydrogenetic ferromanganese crusts. Geochem. J. 43, 37–47.
Bau, M., Koschinsky, A., Dulski, P., Hein, J.R., 1996. Comparison of the partitioning behaviours of yttrium, rare earth elements, and titanium between hydrogenetic marine ferromanganese crusts and seawater. Geochim. Cosmochim. Acta 60, 1709–1725.
Berndt, C., Planke, S., Alvarez Zarikian, C.A., Frieling, J., Jones, M.T., Millett, J.M., Brinkhuis, H., Bünz, S., Svensen, H.H., Longman, J., Scherer, R.P., Karstens, J., Manton, B., Nelissen, M., Reed, B., Faleide, J.I., Huismans, R.S., Agarwal, A., Andrews, G.D.M., Betlem, P., Bhattacharya, J., Chatterjee, S., Christopoulou, M., Clementi, V.J., Ferré, E.C., Filina, I.Y., Guo, P., Harper, D.T., Lambart, S., Mohn, G., Nakaoka, R., Tegner, C., Varela, N., Wang, M., Xu, W., Yager, S.L., 2023. Shallow-water hydrothermal venting linked to the Palaeocene–Eocene Thermal Maximum. Nat. Geosci. 16, 803–809.
Bosboom, R.E., Dupont-Nivet, G., Houben, A.J., Brinkhuis, H., Villa, G., Mandic, O., Stoica, M., Zachariasse, W.J., Guo, Z., Li, C., 2011. Late Eocene sea retreat from the Tarim Basin (west China) and concomitant Asian paleoenvironmental change. Palaeogeogr. Palaeoclimatol. Palaeoecol. 299, 385–398.
Bosboom, R., Dupont-Nivet, G., Grothe, A., Brinkhuis, H., Villa, G., Mandic, O., Stoica, M., Huang, W., Yang, W., Guo, Z., 2014. Linking Tarim Basin sea retreat (west China) and Asian aridification in the late Eocene. Basin Res. 26, 621–640.
Bowen, G.J., 2013. Up in smoke: a role for organic carbon feedbacks in Paleogene hyperthermals. Glob. Planet. Chang. 109, 18–29.
Bowen, G.J., Zachos, J.C., 2010. Rapid carbon sequestration at the termination of the Palaeocene–Eocene Thermal Maximum. Nat. Geosci. 3, 866–869.
Bridgestock, L., Hsieh, Y.-T., Porcelli, D., Henderson, G.M., 2019. Increased export production during recovery from the Paleocene–Eocene thermal maximum constrained by sedimentary Ba isotopes. Earth Planet. Sci. Lett. 510, 53–63.
Byrne, R., Sholkovitz, E., 1996. Marine chemistry and geochemistry of the lanthanides. In: Handbook on the Physics and Chemistry of Rare Earths, 23, pp. 497–593.
Calvert, S., Pedersen, T., 1993. Geochemistry of recent oxic and anoxic marine sediments: implications for the geological record. Mar. Geol. 113, 67–88.
Camuffo, D., 1995. Physical weathering of stones. Sci. Total Environ. 167, 1–14.
Cao, W., Xi, D., Melinte-Dobrinescu, M.C., Jiang, T., Wise Jr., S.W., Wan, X., 2018. Calcareous nannofossil changes linked to climate deterioration during the Paleocene–Eocene thermal maximum in Tarim Basin, NW China. Geosci. Front. 9, 1465–1478.
Carmichael, M.J., Lunt, D.J., Huber, M., Heinemann, M., Kiehl, J., LeGrande, A., Loptson, C.A., Roberts, C.D., Sagoo, N., Shields, C., 2016. A model–model and data–model comparison for the early Eocene hydrological cycle. Clim. Past 12, 455–481.
Carmichael, M.J., Inglis, G.N., Badger, M.P., Naafs, B.D.A., Behrooz, L., Remmelzwaal, S., Monteiro, F.M., Rohrssen, M., Farnsworth, A., Buss, H.L., 2017. Hydrological and

associated biogeochemical consequences of rapid global warming during the Paleocene-Eocene Thermal Maximum. Glob. Planet. Chang. 157, 114–138.
Carmichael, M.J., Pancost, R.D., Lunt, D.J., 2018. Changes in the occurrence of extreme precipitation events at the Paleocene–Eocene thermal maximum. Earth Planet. Sci. Lett. 501, 24–36.
Chaillou, G., Anschutz, P., Lavaux, G., Schäfer, J., Blanc, G., 2002. The distribution of Mo, U, and Cd in relation to major redox species in muddy sediments of the Bay of Biscay. Mar. Chem. 80, 41–59.
Chamley, H., 2013. Clay Sedimentology. Springer Science & Business Media.
Chen, J., An, Z., Head, J., 1999. Variation of Rb/Sr ratios in the loess-paleosol sequences of central China during the last 130,000 years and their implications for monsoon paleoclimatology. Quat. Res. 51, 215–219.
Chen, Z., Ding, Z., Yang, S., Zhang, C., Wang, X., 2016. Increased precipitation and weathering across the Paleocene-Eocene Thermal Maximum in central China. Geochem. Geophys. Geosyst. 17, 2286–2297.
Clarkson, M.O., Lenton, T.M., Andersen, M.B., Bagard, M.-L., Dickson, A.J., Vance, D., 2021. Upper limits on the extent of seafloor anoxia during the PETM from uranium isotopes. Nat. Commun. 12, 1–9.
Colbourn, G., Ridgwell, A., Lenton, T., 2015. The time scale of the silicate weathering negative feedback on atmospheric CO2. Glob. Biogeochem. Cycles 29, 583–596.
Colin, C., Turpin, L., Bertaux, J., Desprairies, A., Kissel, C., 1999. Erosional history of the Himalayan and Burman ranges during the last two glacial–interglacial cycles. Earth Planet. Sci. Lett. 171, 647–660.
Cramwinckel, M.J., Burls, N.J., Fahad, A.A., Knapp, S., West, C.K., Reichgelt, T., Greenwood, D.R., Chan, W.L., Donnadieu, Y., Hutchinson, D.K., 2023. Global and zonal-mean hydrological response to early Eocene warmth. Paleoceanogr. Paleoclimatol. e2022PA004542.
Cui, Y., Kump, L.R., Ridgwell, A.J., Charles, A.J., Junium, C.K., Diefendorf, A.F., Freeman, K.H., Urban, N.M., Harding, I.C., 2011. Slow release of fossil carbon during the Palaeocene-Eocene Thermal Maximum. Nat. Geosci. 4, 481–485.
Dasch, E.J., 1969. Strontium isotopes in weathering profiles, deep-sea sediments, and sedimentary rocks. Geochim. Cosmochim. Acta 33, 1521–1552.
De Carlo, E.H., Wen, X.-Y., Irving, M., 1997. The influence of redox reactions on the uptake of dissolved Ce by suspended Fe and Mn oxide particles. Aquat. Geochem. 3, 357–389.
Deconinck, J.F., Hesselbo, S.P., Pellenard, P., 2019. Climatic and sea-level control of Jurassic (Pliensbachian) clay mineral sedimentation in the Cardigan Bay Basin, Llanbedr (Mochras Farm) borehole, Wales. Sedimentology 66, 2769–2783.
DeConto, R.M., Galeotti, S., Pagani, M., Tracy, D., Schaefer, K., Zhang, T., Pollard, D., Beerling, D.J., 2012. Past extreme warming events linked to massive carbon release from thawing permafrost. Nature 484, 87–91.
Dickens, G.R., O'Neil, J.R., Rea, D.K., Owen, R.M., 1995. Dissociation of oceanic methane hydrate as a cause of the carbon isotope excursion at the end of the Paleocene. Paleoceanography 10, 965–971.
Dickson, A.J., Rees-Owen, R.L., März, C., Coe, A.L., Cohen, A.S., Pancost, R.D., Taylor, K., Shcherbinina, E., 2014. The spread of marine anoxia on the northern Tethys margin during the Paleocene-Eocene Thermal Maximum. Paleoceanography 29, 471–488.
Dickson, A.J., Cohen, A.S., Coe, A.L., Davies, M., Shcherbinina, E.A., Gavrilov, Y.O., 2015. Evidence for weathering and volcanism during the PETM from Arctic Ocean and Peri-Tethys osmium isotope records. Palaeogeogr. Palaeoclimatol. Palaeoecol. 438, 300–307.
Dumitrescu, M., Brassell, S.C., 2005. Biogeochemical assessment of sources of organic matter and paleoproductivity during the early Aptian Oceanic Anoxic Event at Shatsky Rise, ODP Leg 198. Org. Geochem. 36, 1002–1022.
Dunkley Jones, T., Lunt, D.J., Schmidt, D.N., Ridgwell, A., Sluijs, A., Valdes, P.J., Maslin, M., 2013. Climate model and proxy data constraints on ocean warming across the Paleocene-Eocene Thermal Maximum. Earth Sci. Rev. 125, 123–145.
Dypvik, H., Riber, L., Burca, F., Rüther, D., Jargvoll, D., Nagy, J., Jochmann, M., 2011. The Paleocene–Eocene thermal maximum (PETM) in Svalbard—clay mineral and geochemical signals. Palaeogeogr. Palaeoclimatol. Palaeoecol. 302, 156–169.
Fedo, C.M., Wayne Nesbitt, H., Young, G.M., 1995. Unraveling the effects of potassium metasomatism in sedimentary rocks and paleosols, with implications for paleoweathering conditions and provenance. Geology 23, 921–924.
Foreman, B.Z., Heller, P.L., Clementz, M.T., 2012. Fluvial response to abrupt global warming at the Palaeocene/Eocene boundary. Nature 491, 92–95.
Frieling, J., Svensen, H.H., Planke, S., Cramwinckel, M.J., Selnes, H., Sluijs, A., 2016. Thermogenic methane release as a cause for the long duration of the PETM. Proc. Natl. Acad. Sci. 113, 12059–12064.
Frieling, J., Gebhardt, H., Huber, M., Adekeye, O.A., Akande, S.O., Reichart, G.-J., Middelburg, J.J., Schouten, S., Sluijs, A., 2017. Extreme warmth and heat-stressed plankton in the tropics during the Paleocene-Eocene Thermal Maximum. Sci. Adv. 3, e1600891.
Fu, H., Jian, X., Pan, H., 2023. Bias in sediment chemical weathering intensity evaluation: a numerical simulation study. Earth Sci. Rev. 104574.
Garzanti, E., Resentini, A., 2016. Provenance control on chemical indices of weathering (Taiwan river sands). Sediment. Geol. 336, 81–95.
Garzanti, E., Padoan, M., Setti, M., López-Galindo, A., Villa, I.M., 2014. Provenance versus weathering control on the composition of tropical river mud (southern Africa). Chem. Geol. 366, 61–74.
Gibson, T., Bybell, L., Mason, D., 2000. Stratigraphic and climatic implications of clay mineral changes around the Paleocene/Eocene boundary of the northeastern US margin. Sediment. Geol. 134, 65–92.
Gislason, S.R., Oelkers, E.H., Eiriksdottir, E.S., Kardjilov, M.I., Gisladottir, G., Sigfusson, B., Snorrason, A., Elefsen, S., Hardardottir, J., Torssander, P., 2009. Direct evidence of the feedback between climate and weathering. Earth Planet. Sci. Lett. 277, 213–222.
Guo, Y., Yang, S., Su, N., Li, C., Yin, P., Wang, Z., 2018. Revisiting the effects of hydrodynamic sorting and sedimentary recycling on chemical weathering indices. Geochim. Cosmochim. Acta 227, 48–63.
Gupta, S., Kumar, K., 2019. Precursors of the Paleocene–Eocene Thermal Maximum (PETM) in the Subathu Group, NW sub-Himalaya, India. J. Asian Earth Sci. 169, 21–46.
Gutjahr, M., Ridgwell, A., Sexton, P.F., Anagnostou, E., Pearson, P.N., Pälike, H., Norris, R.D., Thomas, E., Foster, G.L., 2017. Very large release of mostly volcanic carbon during the Palaeocene–Eocene Thermal Maximum. Nature 548, 573–577.
Haley, B.A., Klinkhammer, G.P., McManus, J., 2004. Rare earth elements in pore waters of marine sediments. Geochim. Cosmochim. Acta 68, 1265–1279.
Harnois, L., 1988. The CIW index: a new chemical index of weathering. Sediment. Geol. 55, 319–322.
Hayashi, K.-I., Fujisawa, H., Holland, H.D., Ohmoto, H., 1997. Geochemistry of~ 1.9 Ga sedimentary rocks from northeastern Labrador, Canada. Geochim. Cosmochim. Acta 61, 4115–4137.
Haynes, L.L., Hönisch, B., 2020. The seawater carbon inventory at the Paleocene–Eocene Thermal Maximum. Proc. Natl. Acad. Sci. 117, 24088–24095.
Higgins, J.A., Schrag, D.P., 2006. Beyond methane: towards a theory for the Paleocene–Eocene thermal maximum. Earth Planet. Sci. Lett. 245, 523–537.
Horner, T., Little, S., Conway, T., Farmer, J., Hertzberg, J.E., Janssen, D., Lough, A., McKay, J., Tessin, A., Galer, S., 2021. Bioactive trace metals and their isotopes as paleoproductivity proxies: an assessment using GEOTRACES-era data. Glob. Biogeochem. Cycles 35 e2020GB006814.
Ivanovich, M., Harmon, R.S., 1992. Uranium-series disequilibrium: applications to earth, marine, and environmental sciences, p. 2.
Jiang, J., Hu, X., Li, J., BouDagher-Fadel, M., Garzanti, E., 2021. Discovery of the Paleocene-Eocene Thermal Maximum in shallow-marine sediments of the Xigaze forearc basin, Tibet: A record of enhanced extreme precipitation and siliciclastic sediment flux. Palaeogeogr. Palaeoclimatol. Palaeoecol. 562, 110095.
Jiang, J., Hu, X., Li, J., Garzanti, E., Jiang, S., Cui, Y., Wang, Y., 2023. Eustatic change across the Paleocene-Eocene Thermal Maximum in the epicontinental Tarim seaway. Glob. Planet. Chang. 229, 104241.
John, C.M., Bohaty, S.M., Zachos, J.C., Sluijs, A., Gibbs, S., Brinkhuis, H., Bralower, T.J., 2008. North American continental margin records of the Paleocene-Eocene thermal maximum: implications for global carbon and hydrological cycling. Paleoceanography 23.
John, C.M., Banerjee, N.R., Longstaffe, F.J., Sica, C., Law, K.R., Zachos, J.C., 2012. Clay assemblage and oxygen isotopic constraints on the weathering response to the Paleocene-Eocene thermal maximum, east coast of North America. Geology 40, 591–594.
Jones, T.D., Lunt, D.J., Schmidt, D.N., Ridgwell, A., Sluijs, A., Valdes, P.J., Maslin, M., 2013. Climate model and proxy data constraints on ocean warming across the Paleocene–Eocene Thermal Maximum. Earth Sci. Rev. 125, 123–145.
Jones, S.M., Hoggett, M., Greene, S.E., Dunkley Jones, T., 2019. Large Igneous Province thermogenic greenhouse gas flux could have initiated Paleocene-Eocene Thermal Maximum climate change. Nat. Commun. 10, 1–16.
Jones, M.T., Stokke, E.W., Rooney, A.D., Frieling, J., Pogge von Strandmann, P.A.E., Wilson, D.J., Svensen, H.H., Planke, S., Adatte, T., Thibault, N.R., Vickers, M.L., Mather, T.A., Tegner, C., Zuchuat, V., Schultz, B.P., 2023. Tracing North Atlantic volcanism and seaway connectivity across the Paleocene–Eocene Thermal Maximum (PETM). Clim. Past 19, 1623–1652.
Katz, M.E., Cramer, B.S., Mountain, G.S., Katz, S., Miller, K.G., 2001. Uncorking the bottle: What triggered the Paleocene/Eocene thermal maximum methane release? Paleoceanography 16, 549–562.
Kaya, M.Y., Dupont-Nivet, G., Frieling, J., Fioroni, C., Rohrmann, A., Altıner, S.Ö., Vardar, E., Tanyaş, H., Mamtimin, M., Zhaojie, G., 2022. The Eurasian epicontinental sea was an important carbon sink during the Palaeocene-Eocene thermal maximum. Commun. Earth Environ. 3, 124.
Kiehl, J.T., Shields, C.A., 2013. Sensitivity of the Palaeocene–Eocene Thermal Maximum climate to cloud properties. Philos. Trans. R. Soc. A Math. Phys. Eng. Sci. 371, 20130093.
Kirtland Turner, S., Hull, P.M., Kump, L.R., Ridgwell, A., 2017. A probabilistic assessment of the rapidity of PETM onset. Nat. Commun. 8, 1–10.
Komar, N., Zeebe, R.E., 2017. Redox-controlled carbon and phosphorus burial: a mechanism for enhanced organic carbon sequestration during the PETM. Earth Planet. Sci. Lett. 479, 71–82.
Kump, L.R., Brantley, S.L., Arthur, M.A., 2000. Chemical weathering, atmospheric CO2, and climate. Annu. Rev. Earth Planet. Sci. 28, 611–667.
Kurtz, A., Kump, L., Arthur, M., Zachos, J., Paytan, A., 2003. Early Cenozoic decoupling of the global carbon and sulfur cycles. Paleoceanography 18.
Kwon, E.Y., Timmermann, A., Tipple, B.J., Schmittner, A., 2022. Projected reversal of oceanic stable carbon isotope ratio depth gradient with continued anthropogenic carbon emissions. Commun. Earth Environ. 3, 62.
Lawrence, M.G., Greig, A., Collerson, K.D., Kamber, B.S., 2006. Rare earth element and yttrium variability in South East Queensland waterways. Aquat. Geochem. 12, 39–72.
Li, G., Hartmann, J., Derry, L.A., West, A.J., You, C.-F., Long, X., Zhan, T., Li, L., Li, G., Qiu, W., 2016. Temperature dependence of basalt weathering. Earth Planet. Sci. Lett. 443, 59–69.
Li, J., Hu, X., Garzanti, E., BouDagher-Fadel, M., 2017. Shallow-water carbonate responses to the Paleocene–Eocene thermal maximum in the Tethyan Himalaya (southern Tibet): Tectonic and climatic implications. Palaeogeogr. Palaeoclimatol. Palaeoecol. 466, 153–165.
Lyons, S.L., Baczynski, A.A., Babila, T.L., Bralower, T.J., Hajek, E.A., Kump, L.R., Polites, E.G., Self-Trail, J.M., Trampush, S.M., Vornlocher, J.R., 2019.

Palaeocene–Eocene thermal maximum prolonged by fossil carbon oxidation. Nat. Geosci. 12, 54–60.
Ma, Z., Gray, E., Thomas, E., Murphy, B., Zachos, J., Paytan, A., 2014. Carbon sequestration during the Palaeocene–Eocene Thermal Maximum by an efficient biological pump. Nat. Geosci. 7, 382–388.
Matsumoto, R., 1995. Causes of the ˆ 1ˆ 3C anomalies of carbonates and a new paradigm'Gas-Hydrate Hypothesis'. J. Geol. Soc. Japan 101, 902–924.
McInerney, F.A., Wing, S.L., 2011. The Paleocene-Eocene Thermal Maximum: a perturbation of carbon cycle, climate, and biosphere with implications for the future. Annu. Rev. Earth Planet. Sci. 39, 489–516.
McLennan, S.M., 1993. Weathering and global denudation. J. Geol. 101, 295–303.
McLennan, S.M., 1994. Rare earth element geochemistry and the "tetrad" effect. Geochim. Cosmochim. Acta 58, 2025–2033.
Mclennan, S.M., 2018. Rare Earth Elements in Sedimentary Rocks: Influence of Provenance and Sedimentary Processes. In: Geochemistry and Mineralogy of rare Earth Elements. De Gruyter, pp. 169–200.
McLennan, S., Hemming, S., McDaniel, D., Hanson, G., 1993. Geochemical approaches to sedimentation, provenance, and tectonics. Special Papers-Geological Society of America, 284, pp. 21–40.
McManus, J., Berelson, W.M., Klinkhammer, G.P., Hammond, D.E., Holm, C., 2005. Authigenic uranium: relationship to oxygen penetration depth and organic carbon rain. Geochimica et Cosmichimica Acta 69, 95–108.
Meunier, A., Velde, B., Velde, B., 2004. Illite: Origins, Evolution and Metamorphism. Springer Science & Business Media.
Moore, D.M., Reynolds Jr., R.C., 1989. X-ray Diffraction and the Identification and Analysis of Clay Minerals. Oxford University Press (OUP).
Morford, J.L., Emerson, S.R., Breckel, E.J., Kim, S.H., 2005. Diagenesis of oxyanions (V, U, Re, and Mo) in pore waters and sediments from a continental margin. Geochim. Cosmochim. Acta 69, 5021–5032.
Murphy, B., Farley, K., Zachos, J., 2010. An extraterrestrial 3He-based timescale for the Paleocene–Eocene thermal maximum (PETM) from Walvis Ridge, IODP Site 1266. Geochim. Cosmochim. Acta 74, 5098–5108.
Nesbitt, H., Young, G., 1982. Early Proterozoic climates and plate motions inferred from major element chemistry of lutites. Nature 299, 715–717.
Nesbitt, H., Martini, I., Chesworth, W., 1992. Diagenesis and metasomatism of weathering profile, with emphasis on Precambrian paleosols. In: Weathering, Soils & Paleosols, pp. 127–152.
Pagani, M., Pedentchouk, N., Huber, M., Sluijs, A., Schouten, S., Brinkhuis, H., Sinninghe Damsté, J.S., Dickens, G.R., 2006. Arctic hydrology during global warming at the Palaeocene/Eocene thermal maximum. Nature 442, 671–675.
Panahi, A., Young, G.M., Rainbird, R.H., 2000. Behavior of major and trace elements (including REE) during Paleoproterozoic pedogenesis and diagenetic alteration of an Archean granite near Ville Marie, Quebec, Canada. Geochim. Cosmochim. Acta 64, 2199–2220.
Papadomanolaki, N.M., Sluijs, A., Slomp, C.P., 2022. Eutrophication and deoxygenation forcing of marginal marine organic carbon burial during the PETM. Paleoceanogr. Paleoclimatol. 37 e2021PA004232.
Penman, D.E., 2016. Silicate weathering and North Atlantic silica burial during the Paleocene-Eocene Thermal Maximum. Geology 44, 731–734.
Perri, F., 2018. Reconstructing chemical weathering during the Lower Mesozoic in the Western-Central Mediterranean area: a review of geochemical proxies. Geol. Mag. 155, 944–954.
Pogge von Strandmann, P.A., Jones, M.T., West, A.J., Murphy, M.J., Stokke, E.W., Tarbuck, G., Wilson, D.J., Pearce, C.R., Schmidt, D.N., 2021. Lithium isotope evidence for enhanced weathering and erosion during the Paleocene-Eocene Thermal Maximum. Sci. Adv. 7, eabh4224.
Pourmand, A., Dauphas, N., Ireland, T.J., 2012. A novel extraction chromatography and MC-ICP-MS technique for rapid analysis of REE, Sc and Y: revising CI-chondrite and Post-Archean Australian Shale (PAAS) abundances. Chem. Geol. 291, 38–54.
Rahi, I., Sharma, A., Yadav, M., Ali, S., Naik, A.S., 2022. Monsoon Pattern Changes along PETM Recorded in the Barmer Basin, Rajasthan, India, AGU Fall Meeting Abstracts. PP42E-1150.
Reolid, M., Rodríguez-Tovar, F.J., Marok, A., Sebane, A., 2012. The Toarcian oceanic anoxic event in the Western Saharan Atlas, Algeria (North African paleomargin): role of anoxia and productivity. Bulletin 124, 1646–1664.
Robert, C., Kennett, J.P., 1994. Antarctic subtropical humid episode at the Paleocene-Eocene boundary: clay-mineral evidence. Geology 22, 211–214.
Röhl, U., Westerhold, T., Bralower, T.J., Zachos, J.C., 2007. On the duration of the Paleocene-Eocene thermal maximum (PETM). Geochem. Geophys. Geosyst. 8.
Scheffler, K., Buehmann, D., Schwark, L., 2006. Analysis of late Palaeozoic glacial to postglacial sedimentary successions in South Africa by geochemical proxies–response to climate evolution and sedimentary environment. Palaeogeogr. Palaeoclimatol. Palaeoecol. 240, 184–203.
Schlegel, A., Lisker, F., Dörr, N., Jochmann, M., Schubert, K., Spiegel, C., 2013. Petrography and geochemistry of siliciclastic rocks from the Central Tertiary Basin of Svalbard–implications for provenance, tectonic setting and climate. Z. Dtsch. Ges. Geowiss. 164, 173–186.
Schmitz, B., Pujalte, V., 2007. Abrupt increase in seasonal extreme precipitation at the Paleocene-Eocene boundary. Geology 35, 215–218.
Schoepfer, S.D., Shen, J., Wei, H., Tyson, R.V., Ingall, E., Algeo, T.J., 2015. Total organic carbon, organic phosphorus, and biogenic barium fluxes as proxies for paleomarine productivity. Earth Sci. Rev. 149, 23–52.
Schoon, P.L., Heilmann-Clausen, C., Schultz, B.P., Damsté, J.S.S., Schouten, S., 2015. Warming and environmental changes in the eastern North Sea Basin during the Palaeocene–Eocene Thermal Maximum as revealed by biomarker lipids. Org. Geochem. 78, 79–88.
Self-Trail, J.M., Robinson, M.M., Bralower, T.J., Sessa, J.A., Hajek, E.A., Kump, L.R., Trampush, S.M., Willard, D.A., Edwards, L.E., Powars, D.S., 2017. Shallow marine response to global climate change during the Paleocene-Eocene Thermal Maximum, Salisbury Embayment, USA. Paleoceanography 32, 710–728.
Shen, J., Schoepfer, S.D., Feng, Q., Zhou, L., Yu, J., Song, H., Wei, H., Algeo, T.J., 2015. Marine productivity changes during the end-Permian crisis and Early Triassic recovery. Earth Sci. Rev. 149, 136–162.
Shen, J., Yin, R., Zhang, S., Algeo, T.J., Bottjer, D.J., Yu, J., Xu, G., Penman, D., Wang, Y., Li, L., 2022. Intensified continental chemical weathering and carbon-cycle perturbations linked to volcanism during the Triassic–Jurassic transition. Nat. Commun. 13, 1–10.
Shields, C.A., Kiehl, J.T., Rush, W., Rothstein, M., Snyder, M.A., 2021. Atmospheric rivers in high-resolution simulations of the Paleocene Eocene Thermal Maximum (PETM). Palaeogeogr. Palaeoclimatol. Palaeoecol. 567, 110293.
Shukla, M.K., Sharma, A., 2018. Carbon isotope and REE characteristics of the Paleocene–Eocene shallow marine Subathu formation from the NW Himalaya (India) and their paleo-environmental implications. Geochemistry 78, 314–322.
Sluijs, A., Schouten, S., Pagani, M., Woltering, M., Brinkhuis, H., Damsté, J.S.S., Dickens, G.R., Huber, M., Reichart, G.-J., Stein, R., 2006. Subtropical Arctic Ocean temperatures during the Palaeocene/Eocene thermal maximum. Nature 441, 610–613.
Sluijs, A., Röhl, U., Schouten, S., Brumsack, H.J., Sangiorgi, F., Sinninghe Damsté, J.S., Brinkhuis, H., 2008. Arctic late Paleocene–early Eocene paleoenvironments with special emphasis on the Paleocene-Eocene thermal maximum (Lomonosov Ridge, Integrated Ocean Drilling Program Expedition 302). Paleoceanography 23.
Sluijs, A., Bijl, P.K., Schouten, S., Röhl, U., Reichart, G.-J., Brinkhuis, H., 2011. Southern ocean warming, sea level and hydrological change during the Paleocene-Eocene thermal maximum. Clim. Past 7, 47–61.
Stirling, C.H., Andersen, M.B., Potter, E.-K., Halliday, A.N., 2007. Low-temperature isotopic fractionation of uranium. Earth Planet. Sci. Lett. 264, 208–225.
Stokke, E.W., Jones, M.T., Riber, L., Haflidason, H., Midtkandal, I., Schultz, B.P., Svensen, H.H., 2020. Rapid and sustained environmental responses to global warming: the Paleocene–Eocene Thermal Maximum in the eastern North Sea. Clim. Past Discuss. 2020, 1–38.
Storey, M., Duncan, R.A., Swisher III, C.C., 2007. Paleocene-Eocene thermal maximum and the opening of the northeast Atlantic. Science 316, 587–589.
Svensen, H., Planke, S., Malthe-Sorenssen, A., Jamtveit, B., Myklebust, R., Eidem, T.R., Rey, S.S., 2004. Release of methane from a volcanic basin as a mechanism for initial Eocene global warming. Nature 429, 542–545.
Svensen, H., Planke, S., Corfu, F., 2010. Zircon dating ties NE Atlantic sill emplacement to initial Eocene global warming. J. Geol. Soc. 167, 433–436.
Takahashi, S., Yamasaki, S.-I., Ogawa, Y., Kimura, K., Kaiho, K., Yoshida, T., Tsuchiya, N., 2014. Bioessential element-depleted ocean following the euxinic maximum of the end-Permian mass extinction. Earth Planet. Sci. Lett. 393, 94–104.
Tanaka, E., Yasukawa, K., Ohta, J., Kato, Y., 2022. Enhanced continental chemical weathering during the multiple early Eocene hyperthermals: new constraints from the southern Indian Ocean. Geochim. Cosmochim. Acta. 331, 192–211.
Tateo, F., 2020. Clay minerals at the paleocene–eocene thermal maximum: interpretations, limits, and perspectives. Minerals 10, 1073.
Tierney, J.E., Zhu, J., Li, M., Ridgwell, A., Hakim, G.J., Poulsen, C.J., Whiteford, R.D., Rae, J.W., Kump, L.R., 2022. Spatial patterns of climate change across the Paleocene–Eocene Thermal Maximum. Proc. Natl. Acad. Sci. 119, e2205326119.
Tribovillard, N., Algeo, T.J., Lyons, T., Riboulleau, A., 2006. Trace metals as paleoredox and paleoproductivity proxies: an update. Chem. Geol. 232, 12–32.
Wang, S.-L., Shu, L.-S., Zhu, W.-B., Xu, M.-J., Lu, H.-F., Xiao, Z.-Y., Luo, J.-C., Zhu, C.-J., 2012. Mesozoic faults in the NE Tarim (western China) and the implications on collisions in the southern Eurasian margin. J. Asian Earth Sci. 56, 191–199.
Wang, Y., Cui, Y., Su, H., Jiang, J., Wang, Y., Yang, Z., Hu, X., Jiang, S., 2022. Response of calcareous nannoplankton to the Paleocene–Eocene Thermal Maximum in the Paratethys Seaway (Tarim Basin, West China). Glob. Planet. Chang. 217, 103918.
Wedepohl, K., 1971. Environmental influences on the chemical composition of shales and clays. Phys. Chem. Earth 8, 307–333.
Wedepohl, K., 1991. The composition of the upper earth's crust and the natural cycles of selected metals. Metal in natural raw materials, natural resources. Metals and their compounds in the environment. Occurrence, Analysis and Biological Relevance, pp. 3–17.
Wei, L., Xiumian, H., Melinte-Dobrinescu, M., 2021. Early Paleogene hyperthermal events and their environmental impacts in Qimugen section, Tarim Sea. Chin. Sci. Bull. 66, 1067–1082.
West, A.J., Galy, A., Bickle, M., 2005. Tectonic and climatic controls on silicate weathering. Earth Planet. Sci. Lett. 235, 211–228.
Wieczorek, R., Fantle, M.S., Kump, L.R., Ravizza, G., 2013. Geochemical evidence for volcanic activity prior to and enhanced terrestrial weathering during the Paleocene Eocene Thermal Maximum. Geochim. Cosmochim. Acta 119, 391–410.
Xi, D., Cao, W., Cheng, Y., Jiang, T., Jia, J., Li, Y., Wan, X., 2016. Late Cretaceous biostratigraphy and sea-level change in the southwest Tarim Basin. Palaeogeogr. Palaeoclimatol. Palaeoecol. 441, 516–527.
Xiao, W.-J., Zhang, L.-C., Qin, K.-Z., Sun, S., Li, J.-L., 2004. Paleozoic accretionary and collisional tectonics of the Eastern Tianshan (China): implications for the continental growth of central Asia. Am. J. Sci. 304, 370–395.
Xiong, Z., Li, T., Algeo, T., Nan, Q., Zhai, B., Lu, B., 2012. Paleoproductivity and paleoredox conditions during late Pleistocene accumulation of laminated diatom mats in the tropical West Pacific. Chem. Geol. 334, 77–91.
Xu, H., Liu, B., Wu, F., 2010. Spatial and temporal variations of Rb/Sr ratios of the bulk surface sediments in Lake Qinghai. Geochem. Trans. 11, 1–8.

Yao, W., Paytan, A., Wortmann, U.G., 2018. Large-scale ocean deoxygenation during the Paleocene-Eocene Thermal Maximum. Science 361, 804–806.
Yin, A., Harrison, T.M., 2000. Geologic evolution of the Himalayan-Tibetan orogen. Annu. Rev. Earth Planet. Sci. 28, 211–280.
Zachos, J.C., Röhl, U., Schellenberg, S.A., Sluijs, A., Hodell, D.A., Kelly, D.C., Thomas, E., Nicolo, M., Raffi, I., Lourens, L.J., 2005. Rapid acidification of the ocean during the Paleocene-Eocene thermal maximum. science 308, 1611–1615.
Zeebe, R.E., Zachos, J.C., Dickens, G.R., 2009. Carbon dioxide forcing alone insufficient to explain Palaeocene–Eocene Thermal Maximum warming. Nat. Geosci. 2, 576–580.
Zeebe, R.E., Ridgwell, A., Zachos, J.C., 2016. Anthropogenic carbon release rate unprecedented during the past 66 million years. Nat. Geosci. 9, 325–329.
Zhang, S., Hu, X., Han, Z., Li, J., Garzanti, E., 2018. Climatic and tectonic controls on Cretaceous-Palaeogene sea-level changes recorded in the Tarim epicontinental sea. Palaeogeogr. Palaeoclimatol. Palaeoecol. 501, 92–110.
Zhao, M.-Y., Zheng, Y.-F., 2015. The intensity of chemical weathering: geochemical constraints from marine detrital sediments of Triassic age in South China. Chem. Geol. 391, 111–122.
Zhou, X., Thomas, E., Rickaby, R.E., Winguth, A.M., Lu, Z., 2014. I/Ca evidence for upper ocean deoxygenation during the PETM. Paleoceanography 29, 964–975.
Zhou, L., Friis, H., Poulsen, M.L.K., 2015. Geochemical evaluation of the late Paleocene and early Eocene shales in Siri Canyon, Danish-Norwegian basin. Mar. Pet. Geol. 61, 111–122.
Zhou, X., Thomas, E., Winguth, A., Ridgwell, A., Scher, H., Hoogakker, B.A., Rickaby, R., Lu, Z., 2016. Expanded oxygen minimum zones during the late Paleocene-early Eocene: hints from multiproxy comparison and ocean modeling. Paleoceanography 31, 1532–1546.
Zhu, J., Poulsen, C.J., Tierney, J.E., 2019. Simulation of Eocene extreme warmth and high climate sensitivity through cloud feedbacks. Sci. Adv. 5, eaax1874.
Zimmermann, U., Bahlburg, H., 2003. Provenance analysis and tectonic setting of the Ordovician clastic deposits in the southern Puna Basin, NW Argentina. Sedimentology 50, 1079–1104.